Chapter 5

Simulation results

5.1 Introduction

The mill simulator is constructed out of various models implemented in a C++ environment. The simulator consists of different models as discussed in chapter 3 and 4. Not all of these models can function independently. The roll gap model functions as an independent unit, and as was remarked in section 4.8 the tension and roll gap model form an integrated unit. The nonlinear state space combination of the hydraulic systems and the rolling mill stand also function as an independent unit, which uses the roll gap model in order to provide simulated behaviour of the strip in the roll gap.

As part of the initial investigation a linear control model will be identified by doing System Identification (SID) on the nonlinear mill simulator at a specific operating point. The choice of this operating point is discussed in section 4.2.2.

The input-output (I/O) relationships of the plant/simulator are shown in figure 5.1. The controlled and manipulated variables as well as the plant external plant disturbance, entrance thickness are indicated. The use of these variables in the identification process of a linear plant model, will be discussed in the latter part of this chapter.

The implicit and nonlinear behaviour of the Steckel hot rolling process were discussed in chapters 3 and 4. An algebraic linearization might prove insufficient to capture implicit process behaviour, for example the influence of the deformed roll radius on the calculation of P' in the roll gap model. SID as a means of obtaining models for real plant processes is not uncommon in the industry [15, 80] where the practical data, obtained from the application of step tests or Pseudo Random Binary Signals (PRBS) to the plant, are analysed. This SID approach was also successfully used for the identification of linear models for controller design. Examples of the application of SID to nonlinear plant simulators to find linear models, are the dissertation by F.R. Camisani-Calzolari [23], where speed disturbance rejection controllers for the secondary cooling zone in a continuous caster were

designed, and various rolling mill projects [21, 81]. To algebraically linearize the total rolling process model, which exhibits a number of iterative loops as part of the numerical solution method, can be time consuming and less accurate in comparison to the application of step tests and the use of SID.

5.2 Roll gap model simulations

In this section three figures (figures 5.2, 5.3 and 5.4) are discussed. The results were obtained from three separate simulations of the roll gap model. The settings for these simulations are shown in table 5.1 and will now be further discussed.

Table 5.1: Settings of the input variables of the roll gap model.

Case	$\delta(mm)$	$T_1(MN)$	$T_2(MN)$
1	3	0	0
2	3	5	0
1	3	0	5

In figure 5.2 the vertical roll pressure as a function of the length of the arc of contact is shown, as obtained from simulations conducted using the roll gap model. The shape of the function resembles

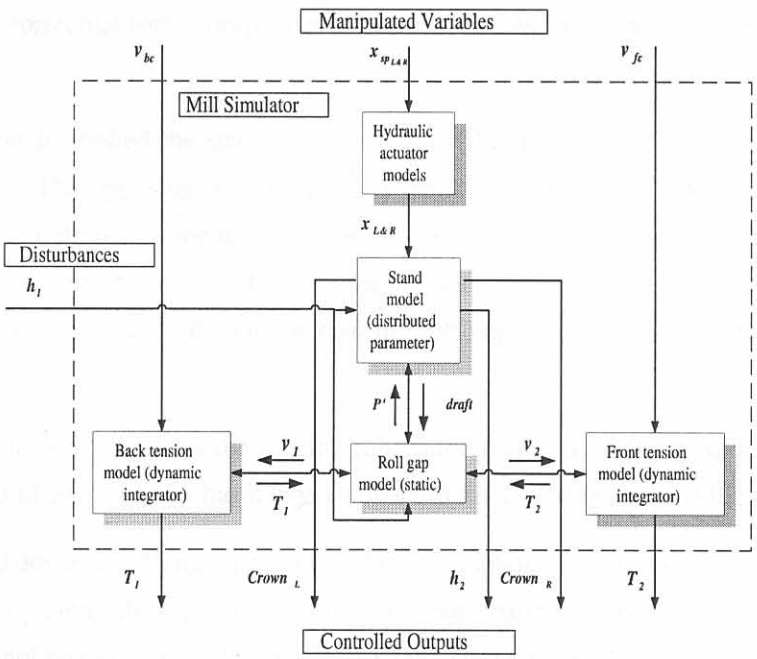

Figure 5.1: The I/O relationship of the plant/simulator. In this figure the manipulated variables of the two hydraulic actuators are treated as one manipulated variable. It is noteworthy to mention that h_1 is not the only modelled disturbance that can result in exit gauge deviations, but T_1 and T_2 can also adversely influence the exit thickness. The latter two variables are plant outputs as well as internal disturbances in the simulator.

a hill (friction hill [28, 2, 44]). The pinnacle of this friction hill corresponds to the neutral point as discussed in section 4.3.1. With no applied strip tension the neutral point is almost in the middle of the arc of contact. When tension is applied to the strip it is seen that the neutral point shifts accordingly. The application of front tension moves the neutral point towards the entrance of the roll gap. This is in agreement with statements in [2], and the neutral point can be moved to the exit of the roll gap by applying back tension to the strip.

When back tension is applied to the strip, the friction forces work towards the exit of the roll gap trying to draw the strip through the roll gap. The application of back tension hinders the delivery of strip from the roll gap and a larger friction force working towards the exit of the roll gap is needed to pull the strip through the roll gap. This larger friction force is obtained when the neutral point shifts towards the exit of the roll gap resulting in a longer length of the arc of contact. This longer arc of contact is subjected to the frictional forces working from the roll gap entrance towards the roll gap exit, thus pulling the strip through the roll gap. In [2] it is stated that the tension lowers the friction component of the rolling force. This is the case and can be explained by way of the vertical pressure distribution curve along the arc of contact. This friction hill can be split up into two areas, the first area resembles a rectangular area and the second area is almost triangular in shape. This triangular area resembles the part of the rolling force that is associated with the frictional forces. When tension is applied this triangle area decreases as can be seen in figure 5.2. But it was stated earlier in the paragraph that a larger friction force along the arc of contact is needed to pull the strip through the roll gap. Thus the horizontal force component increases, while the vertical force component decreases P'.

When front tension is applied the strip is almost pulled through the roll gap due to the actions of the applied tension. The opposing reaction force is the friction force that works from the exit of the roll gap towards the entrance of the roll gap along the arc of contact. Thus when the front tension is increased the neutral point has to shift towards the entrance of the roll gap in order to create a larger frictional force working towards the entrance of the roll gap that opposes the effect of the applied front tension.

Both cases of applied tension lower the specific rolling force (see previous paragraph and figure 5.2), but the application of back tension has a larger impact in the lowering of the rolling force [2].

In figure 5.3 speed deviations along the arc of contact are shown. With the application of front tension the speed of the strip along the arc of contact is larger than than the speeds when no tension and only back tension are applied to the strip. This increase can be attributed to the drawing of the strip through the roll gap. The speed along the arc of contact is smaller compared to the other 2 cases (no tension and only front tension applied), when back tension is applied to the strip.

In figure 5.4 half the thickness deviation along the arc of contact for the three cases[1] are shown. It

[1] i) No applied tension; ii) Applied front tension; iii) Applied back tension

appears that the thickness difference due to the application of tension is small. This is expected due to the fact that the magnitude of the applied tension was limited in order to prevent the tension in the strip from exceeding the yield stress of the material. Larger thickness reduction due to the application of tension can be expected, when the applied tension exceeds the yield stress of the material resulting in necking[2] of the strip.

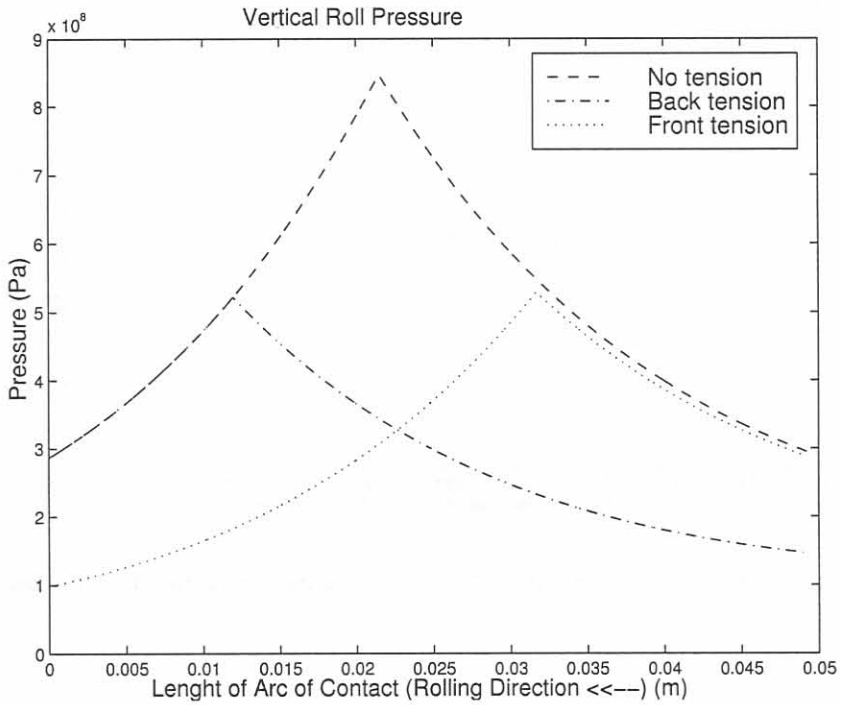

Figure 5.2: Vertical pressure distribution vs. roll gap distance as a function of the applied strip tensions.

In figures 5.5, 5.6, 5.7, and 5.8[3] the draft and the applied tensions are varied in order to investigate how close to the physical limit of the mill the chosen operating point (see section 4.2.2) of the mill simulator is.

From figure 5.8 it can be seen that when the tensions are kept fixed an increase of 2mm in the draft taken is possible. It needs to be stressed that although the mill is capable to handle such an increase the mill frame stretch may be excessive.

From figures 5.5 and 5.6 it can be seen that when the draft increases the specific rolling force increases. The converse is true for increases in the applied strip tensions as can be seen in especially figure 5.7, and also in figures 5.5 and 5.6. The elastic deformation range of the tension process was taken to correspond to 0-200MPa, which is smaller than the calculated yield stress (280MPa) at a draft of 3mm. From figure 5.8 it can be seen that, for a draft of 3mm and applied tensions fixed at their setup values, the specific rolling force is well below the physical limit of the mill.

[2]See section 3.4.2 for a description of necking.

[3]Note that in this section $T_b = T_1$ and $T_f = T_2$ as defined in chapter 3 section 3.4.2.

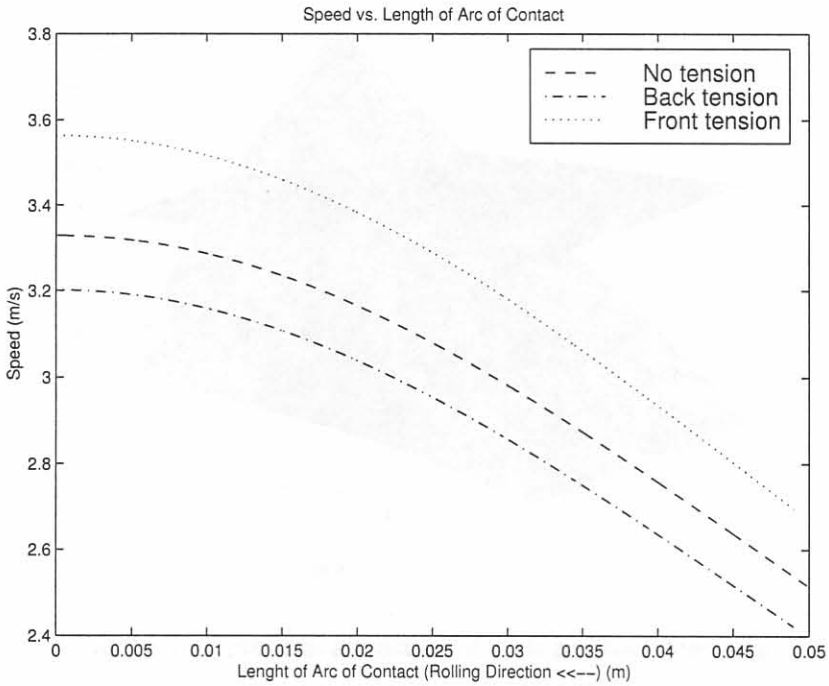

Figure 5.3: Velocity along the arc of contact vs. the length of the arc of contact.

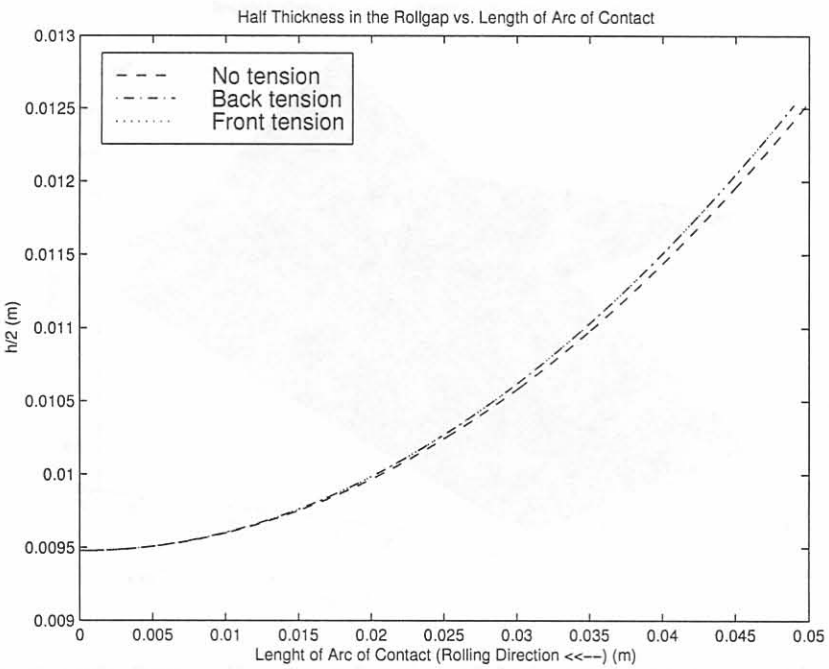

Figure 5.4: Half thickness variation through the roll gap as a function of the length of the arc of contact

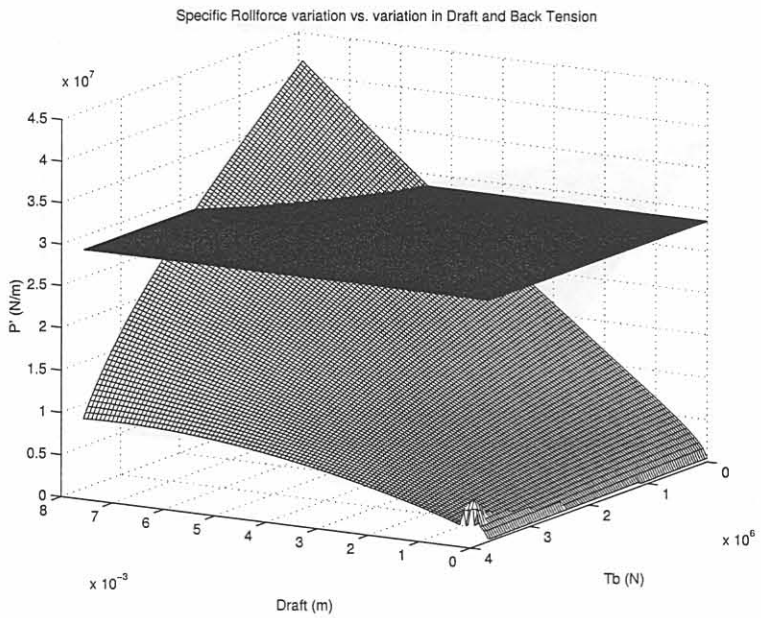

Figure 5.5: The Specific Rolling Force as a function of draft and back tension applied to the rolling mill, when the front tension is kept constant at its setup value ($P' = f(\delta, T_b)|_{T_{f_{setup}}}$). The Physical Mill Limit ($\frac{40MN}{w}|_{w=1.3m} \approx 2.8 \times 10^7 \frac{N}{m}$) is also shown.

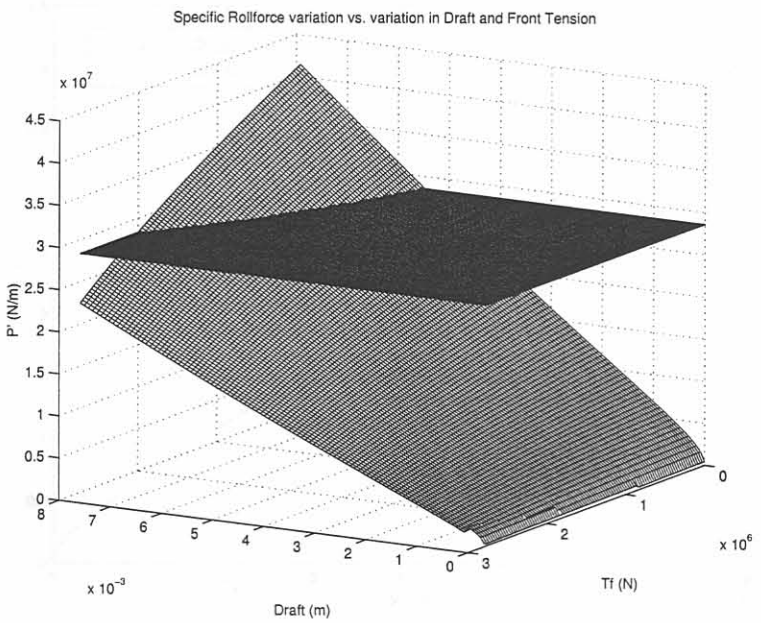

Figure 5.6: The Specific Rolling Force as a function of draft and front tension applied to the rolling mill, when the back tension is kept constant at its setup value ($P' = f(\delta, T_f)|_{T_{b_{setup}}}$). The Physical Mill Limit ($\frac{40MN}{w}|_{w=1.3m} \approx 2.8 \times 10^7 \frac{N}{m}$) is also shown.

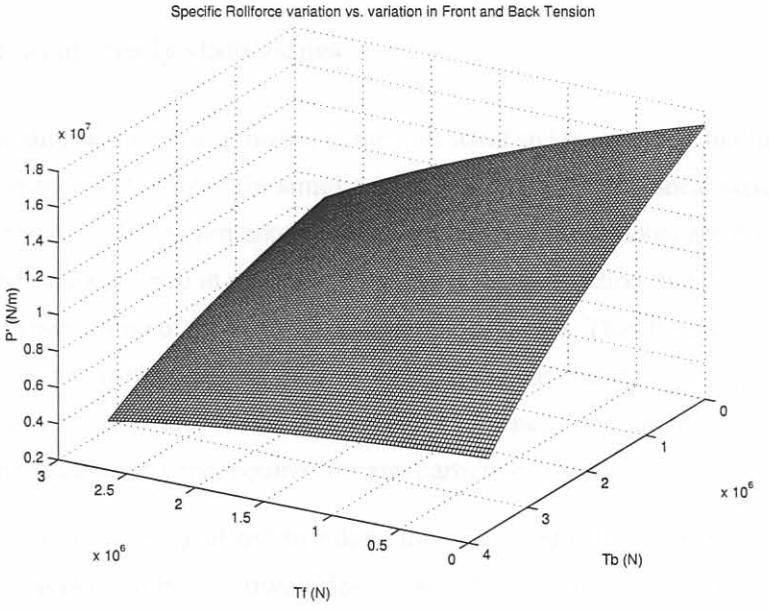

Figure 5.7: The Specific Rolling Force as a function of the applied tensions, when the draft is kept constant at 3mm ($P' = f(T_b, T_f)|_{\delta=3mm}$).

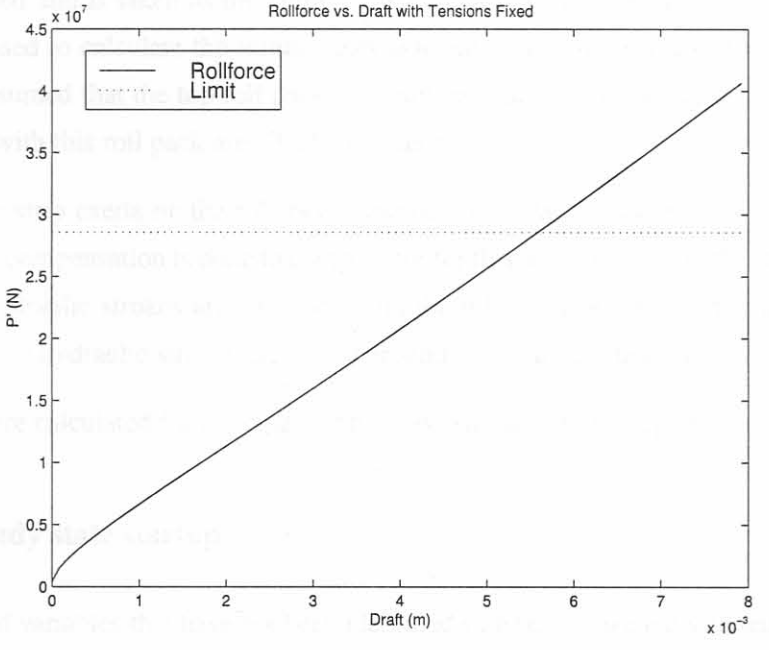

Figure 5.8: The Specific Rolling Force as a function of draft taken, when the tensions are kept constant at their setup values ($P' = f(\delta)|_{T_{b_{setup}}, T_{f_{setup}}}$). The Physical Mill Limit ($\frac{40MN}{w}|_{w=1.3m} \approx 2.8 \times 10^7 \frac{N}{m}$), the horizontal line, is also shown.

5.3 Nonlinear state-space model

5.3.1 Calculation of steady state values

The states of the nonlinear state-space model, of the mill stand and hydraulic actuators, was calculated in order to have a bumpless start up of the simulator. In section 4.7 the nonlinear state-space equations of the simulator are given. It was remarked earlier that most of these states are not defined as small signal variables and that $\mathbf{x}(0) \neq 0$ in general. It is noteworthy to mention that the simulator is started on the acceleration speed ramp of the mill drive synchronous motor. Thus the simulation is not started before commencement of rolling, but rather after a part of the pass has been completed. This start-up procedure is not ideal and the state vector at that instant of time is unknown. This methodology was induced by the long simulation time required for any particular simulation[4].

The states at steady state were calculated by taking the calculated rolling force at $t = 0$. This calculated rolling force was divided by two (two sides of the mill) to yield the shearing forces at the edges of the top roll pack. In the steady state these shearing forces has to equal the thrust forces of the hydraulic actuators. From these thrust forces the pressures in the cylinder chambers can be calculated, by setting the leakage flow between the main chamber and the secondary chamber to zero (e.g. steady state). This implies that the pressures of the main and secondary chambers are equal.

The shearing forces at the edges of the bottom roll pack compresses the load cells. These compressions are calculated and is taken as the vertical displacement of the bottom roll pack. The vertical displacement is used to calculate the initial states associated with the vertical displacements of this roll pack. It is assumed that the top roll pack does not have an initial vertical displacement, and the states associated with this roll pack are all taken as zero.

The force that the strip exerts on the rollers causes the mill to stretch excessively. A static BISRA-Davy gaugemeter compensation is done to compensate for this mill stretch, and the steady state values of the dynamic hydraulic strokes are increased with the relevant compensation quantities, on either side of the mill. The hydraulic strokes are varied around these steady state values.

The states that were calculated for anticipated bumpless simulation start up are shown in table 5.2.

5.3.2 Non steady state startup

The magnitudes of variables that have not been identified satisfactory were discussed in section 4.5.3. The magnitudes are the hydraulic stiffness of the hydraulic jacks (K_J) and the damping between the strip and the work rolls (β_{strip}), which influence the dynamic behaviour of the mill stand, and

[4] An Intel ®Pentium II 400MHz personal computer was used to complete the simulations for this dissertation. Multi-tasked simulations under Windows NT ®ran in excess of 48 hours, which makes it very time consuming to experiment with process parameters.

ultimately the whole process behaviour. A comparison was made between different model scenarios, where the damping coefficient and the hydraulic spring constants, were experimented with. In table 5.3 a representative comparison is made between three different scenarios.

When $K_J = 40e9\frac{N}{m}$, the damping ratios associated with the dominant eigenvalues of the stand model increase and the vibration oscillations decays more rapidly. These increased ratios limit the oscillatory nature of the stand model. The main difference between the models with different β_{strip} is classified according to the degree of bumpless simulation startup. Complete bumpless transfer can not be achieved, because at the time instance when the simulation is started the mill speed is still increasing. In figure 5.10 ($\beta_{strip} = 1e8\frac{N}{m^2.s^{-1}}$) it can be seen that the draft changes quite drastically from the calculated initial state when compared to the model cases where $\beta_{strip} \geq 5e10\frac{N}{m^2.s^{-1}}$ (see figure 5.9).

5.4 System Identification

The proposed controlled variables of the system are the centerline exit thickness of the strip from the roll gap, the tension in the strip whilst rolling on either side of the roll gap, and the thickness profile of the strip. The manipulated variables available are the hydraulic cylinder strokes on both sides of the mill frame and the coiler furnace motor speeds. The hydraulic actuators can function independently or as a combined unit. In figure 5.1 the I/O relationship of the simulator are shown with the manipulated and controlled variables indicated. The linearized plant can be expressed as transfer functions in the

Table 5.2: Calculated states for bumpless simulation start up. The units of the states are not shown.

State	Value
$x_1, x_2, x_5, x_6, x_7, x_8, x_9, x_{10}, x_{12}, x_{13}$	0
x_3	1.84×10^{-6}
x_4	-3.12×10^{-5}
x_7	-3.12×10^{-5}
$x_{11}, x_{14}, x_{15}, x_{16}$	2.15×10^{7}
x_{17}	3.68×10^{-3}
x_{18}	3.65×10^{-3}

Table 5.3: Comparison of the damping ratios (ζ), natural frequencies (ω_n and f_n), and natural period (T_n) for different cases of K_J and β_{strip}.

$K_J(\frac{N}{m})$	$\beta_{strip}(\frac{N}{m^2.s^{-1}})$	ζ	$\omega_n(rad.s^{-1})$	$f_n(Hz)$	$T_n(s)$
0	5e10	1.7700e-009	3.8030e+001	6.0526e+000	1.6522e-001
		1.7700e-009	3.8030e+001	6.0526e+000	1.6522e-001
		1.0000e+000	1.1883e-003	1.8912e-004	5.2876e+003
		1.0000e+000	7.6827e-002	1.2227e-002	8.1783e+001
		6.6661e-003	2.3712e+003	3.7739e+002	2.6498e-003
		6.6661e-003	2.3712e+003	3.7739e+002	2.6498e-003
		1.0000e+000	1.7224e+005	2.7412e+004	3.6480e-005
		1.0000e+000	6.4953e+005	1.0338e+005	9.6734e-006
0	1e8	8.7562e-007	3.8030e+001	6.0526e+000	1.6522e-001
		8.7562e-007	3.8030e+001	6.0526e+000	1.6522e-001
		1.0000e+000	5.9442e-001	9.4605e-002	1.0570e+001
		1.0000e+000	5.6895e+001	9.0551e+000	1.1044e-001
		2.5896e-002	3.3267e+003	5.2946e+002	1.8887e-003
		2.5896e-002	3.3267e+003	5.2946e+002	1.8887e-003
		1.0000e+000	1.1845e+002	1.8851e+001	5.3046e-002
		1.0000e+000	1.2954e+003	2.0616e+002	4.8505e-003
40e9	1e8	8.9491e-003	3.8063e+001	6.0580e+000	1.6507e-001
		8.9491e-003	3.8063e+001	6.0580e+000	1.6507e-001
		5.7559e-002	7.4109e+002	1.1795e+002	8.4783e-003
		5.7559e-002	7.4109e+002	1.1795e+002	8.4783e-003
		2.4562e-002	3.5074e+003	5.5823e+002	1.7914e-003
		2.4562e-002	3.5074e+003	5.5823e+002	1.7914e-003
		1.0000e+000	4.6337e+002	7.3747e+001	1.3560e-002
		1.0000e+000	2.2118e+003	3.5203e+002	2.8407e-003

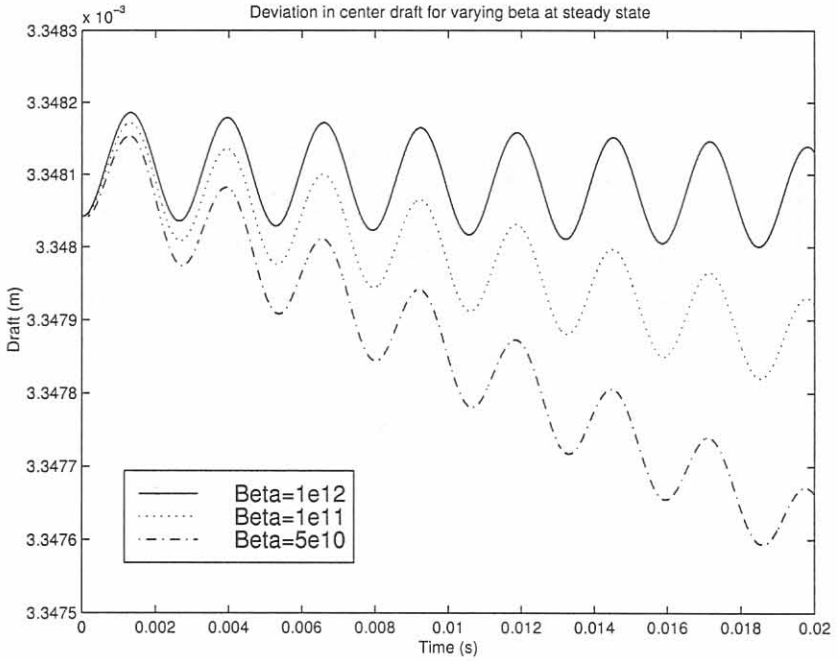

Figure 5.9: Steady state comparison of the draft deviation for $\beta_{strip} \in [5e10, 1e11, 1e12] \frac{N}{m^2.s^{-1}}$ and $K_J = 0 \frac{N}{m}$.

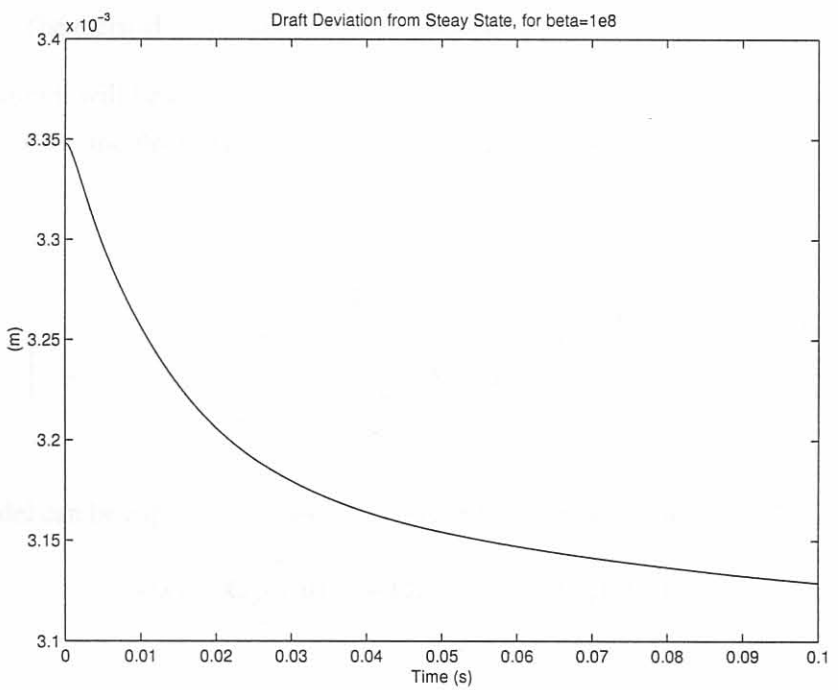

Figure 5.10: Steady state comparison of the draft deviation for $\beta_{strip} = 1e8 \frac{N}{m^2.s^{-1}}$ and $K_J = 0 \frac{N}{m}$.

Laplace transform format as follows:

$$\begin{bmatrix} \delta h_2(s) \\ \delta T_1(s) \\ \delta T_2(s) \\ \delta Cr_L(s) \\ \delta Cr_R(s) \end{bmatrix} = \begin{bmatrix} g_{11}(s) & g_{12}(s) & g_{13}(s) & g_{14}(s) \\ g_{21}(s) & g_{22}(s) & g_{23}(s) & g_{24}(s) \\ g_{31}(s) & g_{32}(s) & g_{33}(s) & g_{34}(s) \\ g_{41}(s) & g_{42}(s) & g_{43}(s) & g_{44}(s) \\ g_{51}(s) & g_{52}(s) & g_{53}(s) & g_{54}(s) \end{bmatrix} \begin{bmatrix} \delta x_{sp_L}(s) \\ \delta x_{sp_R}(s) \\ \delta v_{bc}(s) \\ \delta v_{fc}(s) \end{bmatrix} + \widehat{\mathbf{G}_d}(s) \begin{bmatrix} \delta h_1(s) \\ input\ hardness \\ \mu \\ \delta T_1(s) \\ \delta T_2(s) \\ Cr_{thermal\ rolls} \\ Bearing\ oil\ film \\ Roll\ eccentricity \\ v_{roll} \\ \theta \\ \vdots \end{bmatrix} \tag{5.1}$$

where,

$\widehat{\mathbf{G}_d}(s)$: A matrix containing disturbance transfer functions;

$g_{ij}(s)$: The transfer function between the i^{th} output and j^{th} input;

δCr_L: Strip thickness crown on the left side of the mill;

δCr_R: Strip thickness crown on the right side of the mill

$Cr_{thermal\ rolls}$: The thermal crown build up on the rollers[5].

As a first iteration it will be assumed, similarly to [81], that the hydraulic actuators function jointly. The calculated centerline thickness control signal is applied to each of the actuators.

The reduced model is[6],

$$\begin{bmatrix} \delta h_2(s) \\ \delta T_1(s) \\ \delta T_2(s) \end{bmatrix} = \begin{bmatrix} g_{11}(s) & g_{12}(s) & g_{13}(s) \\ g_{21}(s) & g_{22}(s) & g_{23}(s) \\ g_{31}(s) & g_{32}(s) & g_{33}(s) \end{bmatrix} \begin{bmatrix} \delta x_{sp_{L\&R}}(s) \\ \delta v_{bc}(s) \\ \delta v_{fc}(s) \end{bmatrix} + \begin{bmatrix} g_{d11}(s) & g_{d12}(s) & g_{d13}(s) \\ g_{d21}(s) & 0 & g_{d23}(s) \\ g_{d31}(s) & g_{d32}(s) & 0 \end{bmatrix} \begin{bmatrix} \delta h_1(s) \\ \delta T_1(s) \\ \delta T_2(s) \end{bmatrix} \tag{5.2}$$

The above model can be expressed in standard transfer function model notation [72],

$$\mathbf{y}(s) = \mathbf{G}_p(s)\mathbf{u}(s) + \mathbf{G}_d(s)\mathbf{d}(s) + \mathbf{G}_w(s)\mathbf{w}(s), \tag{5.3}$$

with,

[5] The rest of the variables are either defined in chapter 3 and 4 or are self explanatory.

[6] Only the first row of the disturbance transfer function matrix is considered of importance and the transfer functions $g_{d21}(s), g_{d23}(s), g_{d31}(s), g_{d32}(s)$ will not be identified in this dissertation. It can be argued that the transfer functions $g_{d23}(s), g_{d32}(s) \approx 0$, because the tensions are connected via a static roll gap model.

$\mathbf{y}(s) = \begin{bmatrix} \delta h_2(s) & \delta T_1(s) & \delta T_2(s) \end{bmatrix}^T = \begin{bmatrix} y_1(s) & y_2(s) & y_3(s) \end{bmatrix}^T$: The controlled variable vector;

$\mathbf{u}(s) = \begin{bmatrix} \delta x_{sp_{L\&R}}(s) & \delta v_{bc}(s) & \delta v_{fc}(s) \end{bmatrix}^T = \begin{bmatrix} u_1(s) & u_2(s) & u_3(s) \end{bmatrix}^T$: The manipulated variable vector;

$d(s) = \begin{bmatrix} \delta h_1(s) & \delta T_1(s) & \delta T_2(s) \end{bmatrix}^T$: The measured disturbance vector;

The linear plant model is obtained by applying step tests to one of the three manipulated inputs whilst the other two inputs are kept at their steady state operating points. In the following section the design of these step tests is discussed.

5.4.1 Design and results from the step tests

It was decided to use step tests to identify the linear models. The reason being the ease of their application to the simulator. The application of a PRBS signal might be preferred in industry, because the average energy inserted into the system is zero. The design of a PRBS signal, that capture the necessary dynamics by ensuring that the first zero of the $(\frac{sin(j\omega)}{j\omega})$ frequency envelope of the periodic square wave signal [82] is greater than the plant bandwidth, is difficult in the absence of a given plant bandwidth. Ballpark estimates of the plant bandwidth can however be found from the literature.

When the SID steps are applied to the simulator, the main mill drive speed is forced constant in the simulator at the desired point of linearization in order to eliminate possible dynamic effects on the controlled outputs due to main mill drive speed deviations.

5.4.1.1 Combined hydraulic strokes, $\delta x_{L\&R}$

From figures 5.5, 5.6, and 5.8 it can be seen that another 2 mm of draft increase is permitted before the physical limit of the mill is reached[7]. The linear model that will be identified is for regulation purposes, and it is not anticipated that such a large draft increase will be required, when the mill setup is adapted during the execution of a rolling schedule. A large increase in the mill draft might not even be obtainable due to the significant amount of mill stretch. The magnitude of the hydraulic stroke step was chosen as $1mm$, and from figure 5 in [18] where it is shown that when a supervisory GPC[8]-controller is used to regulate the rolling process after a 1mm hydraulic stroke disturbance was applied. When the controller was switched on after 4 seconds the manipulated stroke was rarely larger than 1mm. Grimble and Katebi [18] state that when the hydraulic stroke was larger than 1mm it was excessive and in this dissertation a dynamic stroke increase range of 1mm was used in the identification of a linear model for process regulation purposes.

[7] It should be stressed that these figures were obtained from simulations using the roll gap and tension model unit of the simulator and the dynamic effects of the rolling mill stand are not reflected in these results.

[8] Generalized Predictive Control.

In figure 5.11 a zoomed plot of the hydraulic strokes of both actuators are shown. When this 2nd order response is approximated as a 1st order response a time constant of $\tau = 83ms$ can be calculated, which corresponds to a bandwidth of 12Hz. This bandwidth corresponds to a benchmark value of 15Hz [1] for hydraulic systems. From figure 20 of [8] it can be concluded that the hydraulic actuators' bandwidth fall into the specified operation range for a double acting position mode hydraulic actuator.

In figure 5.12 the cascaded controlled servovalve-spool strokes are shown. Note the hard limit of $|3mm|$ imposed on the spool stroke movement. This hard limit was introduced by reasoning that the cylinder flow can not increase if the spool opening is already at a maximum. Thus if the gain of the cascaded PI stroke position controllers of the hydraulic systems are tweaked as such that the servovalve spools' limits are readily attained for larger required strokes, the system response will be slower than anticipated due to the flow saturation.

In figures 5.13-5.15 different comparison plots of the exit gauge are shown. In figure 5.13 the supposed steady state evolution of the exit gauge are shown at the strip center and end points. The deviation away from the steady state is attributed to non bumpless start-up as well as the forcing of the strip on the rollers, which is not compensated for.

In figure 5.14 the steady state evolution is compared to the exit gauge response when a combined hydraulic stroke increase of $1mm$ is applied. The relative difference between these two responses is large and constitute the dynamic behaviour due to a hydraulic stroke increase. It is important to note the order with which the thickness decreases compared to the input step of $1mm$. From this figure it can be seen that the thickness decreased with a mere $|300\mu m|$, and the rest of the $1mm$ stroke is

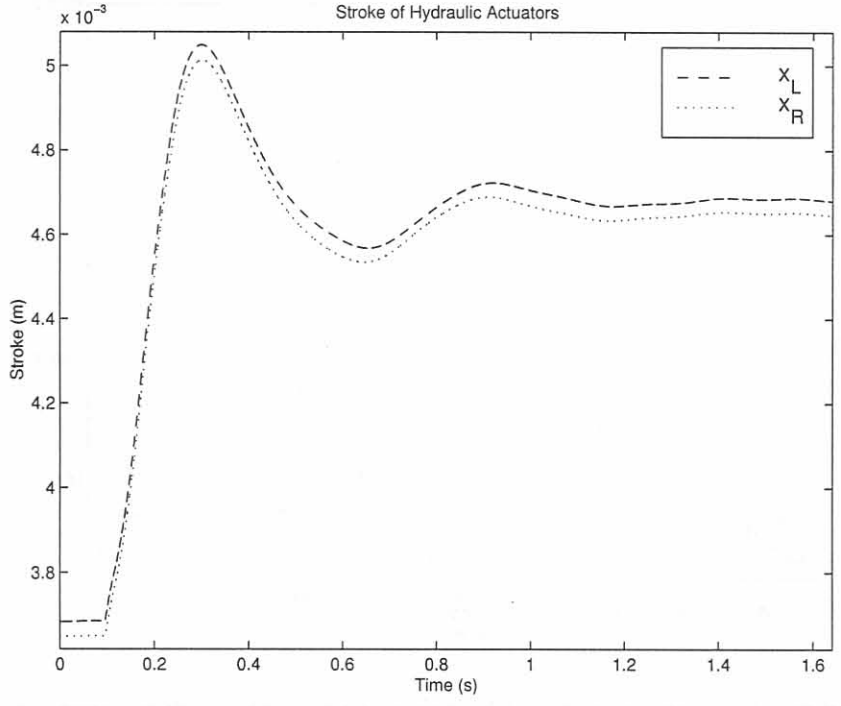

Figure 5.11: Hydraulic strokes, after a step input of 1mm was done in the hydraulic stroke at 92.6ms.

embedded in the mill stretch.

In figure 5.15 a three dimensional view of the exit thickness are shown, after the application of a

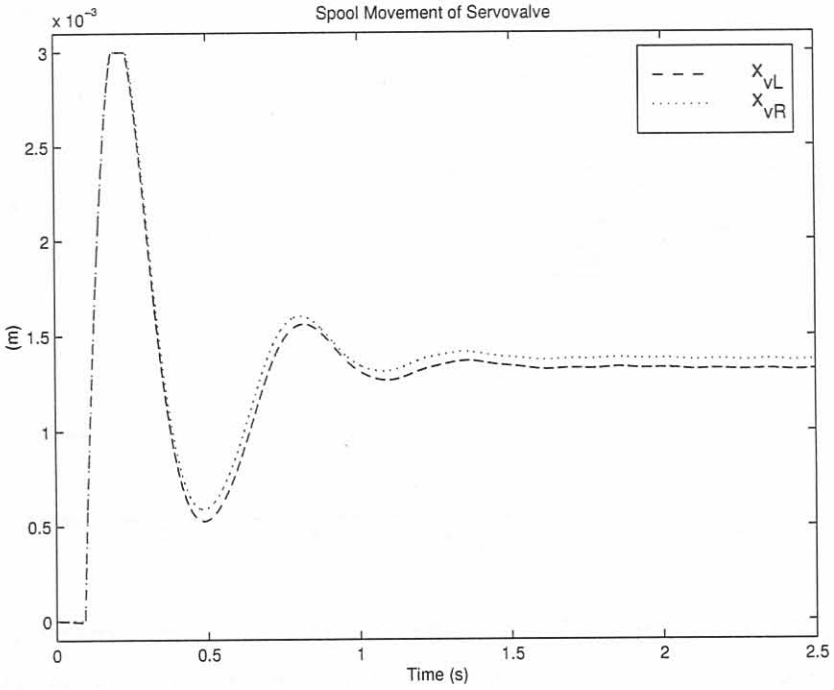

Figure 5.12: Servovalve spool stroke, after a step input of 1mm was done in the hydraulic stroke at 92.6ms.

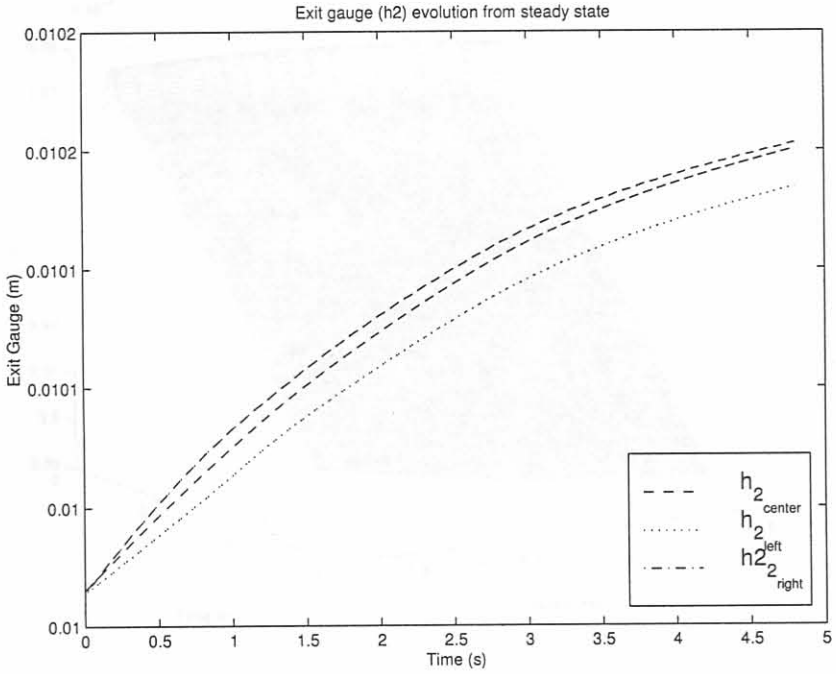

Figure 5.13: Exit gauge at the center and end points of the strip, at supposed steady state (i.e. the manipulated variables are kept zero).

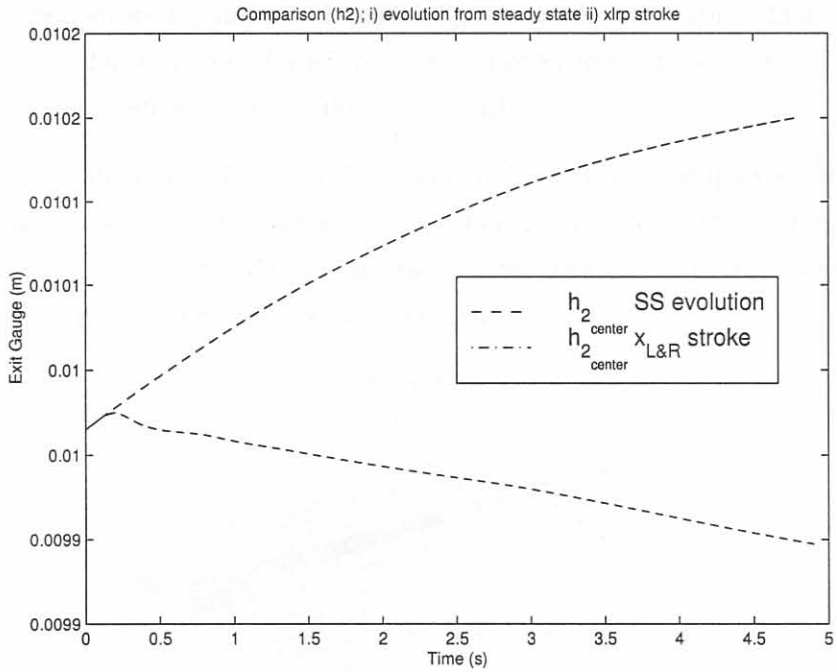

Figure 5.14: A comparison plot of the exit gauge at the center of the strip, between the output obtained when a step input of 1mm was done in the hydraulic stroke at 92.6ms, and the steady state evolution.

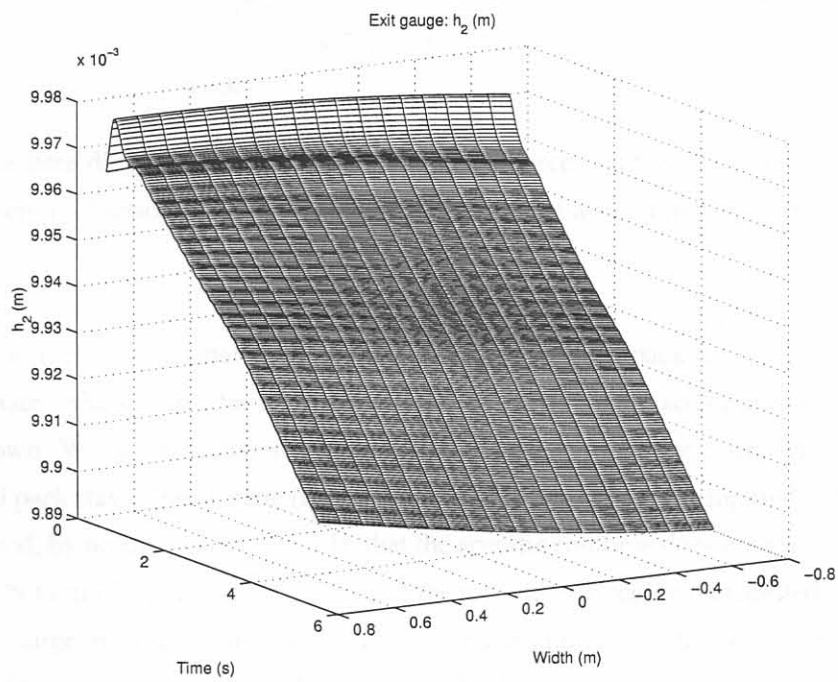

Figure 5.15: A three dimensional view of the exit gauge as a function of space and time, after a step input of 1mm was done in the hydraulic stroke at 92.6ms.

hydraulic stroke setpoint change was made at 92.6ms. The plotted thickness deviations does not reflect the strip's bottom and top surfaces. From this figure the simulator's ability to simulate thickness crown is displayed. There is room for improvement in order to create a superior thickness crown simulator and special mention is made of this in the conclusions.

In figure 5.16 a three dimensional view of the specific rollforce that the strip exerts onto the two roll packs as a function of space and time are shown in response to the 1mm stroke step that was applied. The function is not very smooth and this is attributed to the static nature of the roll gap model. This function is highly nonlinear as was pointed out in chapter 3.

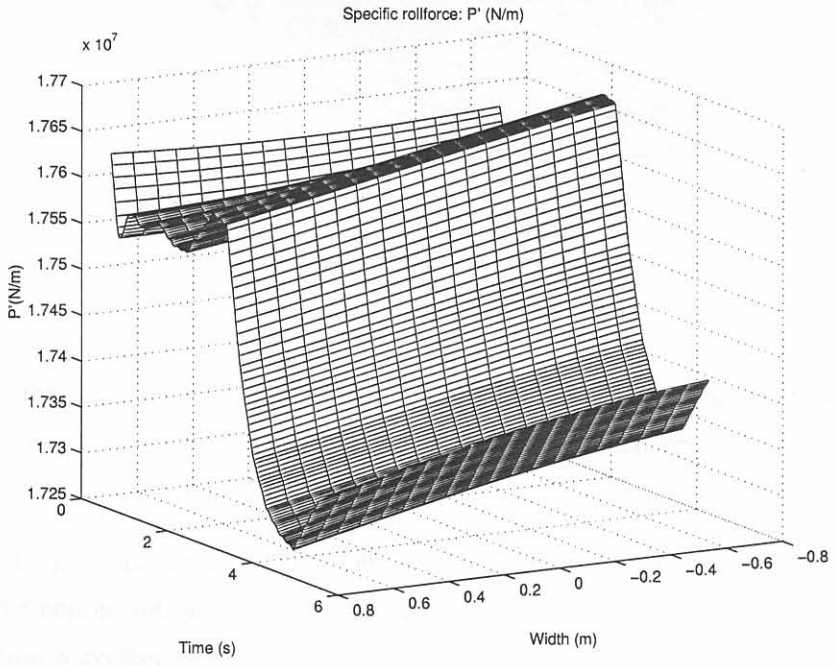

Figure 5.16: A three dimensional view of the specific rollforce that the strip exerts onto the two roll packs as a function of space and time, after the application of a step input of $1mm$ in the hydraulic stroke at 92.6ms.

In figure 5.17 a three dimensional view of the top and bottom roll pack deviation movements from their steady state values, after the application of a hydraulic stroke setpoint change was made at 92.6ms, is shown. When the deviational movements of the roll packs are compared it is evident that the bottom roll pack stays almost static (ignoring the high frequency small amplitude vibrations). This can be explained, by noting from figure 5.16 that the specific rollforce does change over time but not by much. The bottom (K_{LB} and K_{RB}) springs of the mill stand model was modelled as measurement load cells with large associated stiffnesses. This therefore implies that the movement of the bottom roll pack should be minimimal. Note that figure 5.17 reflects the small signal movement of the roll packs and does not imply that the one roll pack moves through the other roll pack. It can be seen from this figure that while the bottom roll pack movement stays almost static, the top roll pack movement is dictated by the hydraulic stroke. The draft deviation from the setup draft is the difference between

the deviation movements of the roll packs, when the input thickness is fixed.

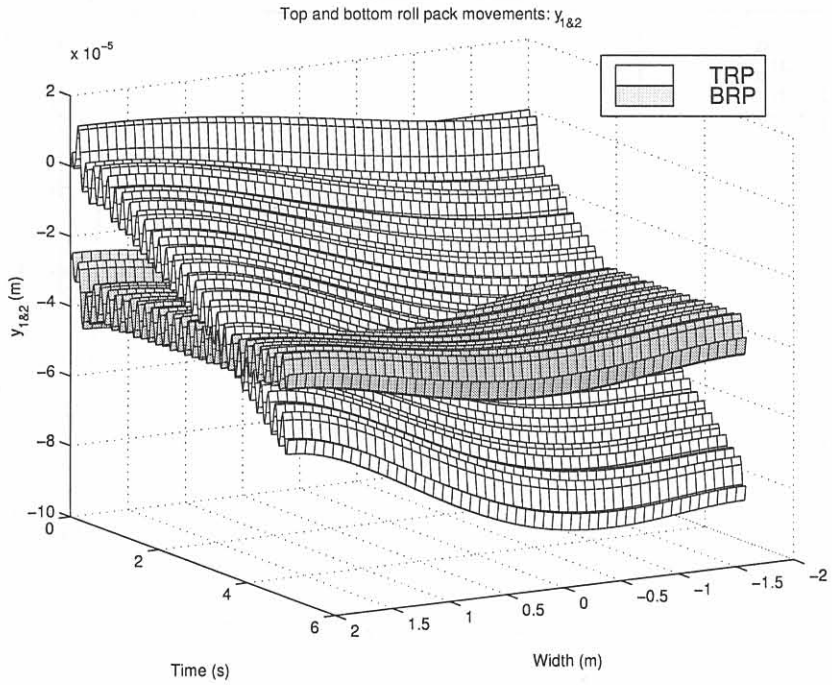

Figure 5.17: A three dimensional view of the deviation movement from the steady state of the two roll packs as functions of space and time, after the application of a step input of $1mm$ in the hydraulic stroke at 92.6ms.

From figure 5.17 it is also observed that the second mode of vibration is the dominant mode of vibration for the bottom roll pack. For the top roll pack a combination of the first and the second mode of vibration is evident.

5.4.1.2 Speed steps, $\delta v_{bc}, \delta v_{fc}$

The speed steps were calculated in order to have the maximum effect on the centerline gauge. This entails increasing the tension, on either side to a maximum stress value of $200MPa \Rightarrow [3.72MN\ |_{h_1=13.3mm}, 2.716MN\ |_{h_2=9.7mm}]$ from the setup values of $\approx$ 8MPa. Tension is not permitted to be negative, because negative tensions will not decrease the rolling force and will according to the roll gap model increase the rolling force. This might not be a true reflection of the true rolling process. The tensions are calculated by integrating the speed difference between the coiler and the roll gap speeds. This knowledge is used to calculate the step size of the coiler speed or the time duration of the step using the following relationship,

$$E_{ss}A_{cross_i}L^{-1}_{rg\leftrightarrow cf}\Delta x_i = E_{ss}A_{cross_i}L^{-1}_{rg\leftrightarrow cf}\Delta v_{\kappa c}\Delta t_{step} = 200\times 10^6 A_{cross_i} - T_{i_{setup}}, \qquad (5.4)$$

where $i \in [1,2]$ and correspondingly $\kappa \in [b,f]$. $E_{ss} = 106GPa$ is Youngs' modulus of stainless steel at $970°C$. A_{cross_i} is the cross sectional area of the sheet perpendicular to the rolling direction on either side of the roll gap.

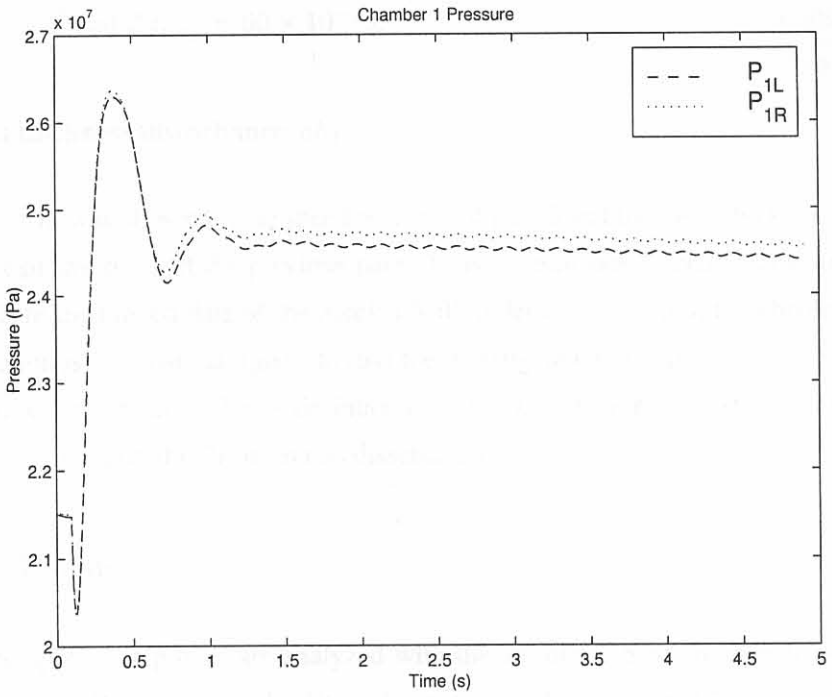

Figure 5.18: Pressure in cylinder chamber 1, after the application of a step input of $1mm$ in the hydraulic stroke at 92.6ms.

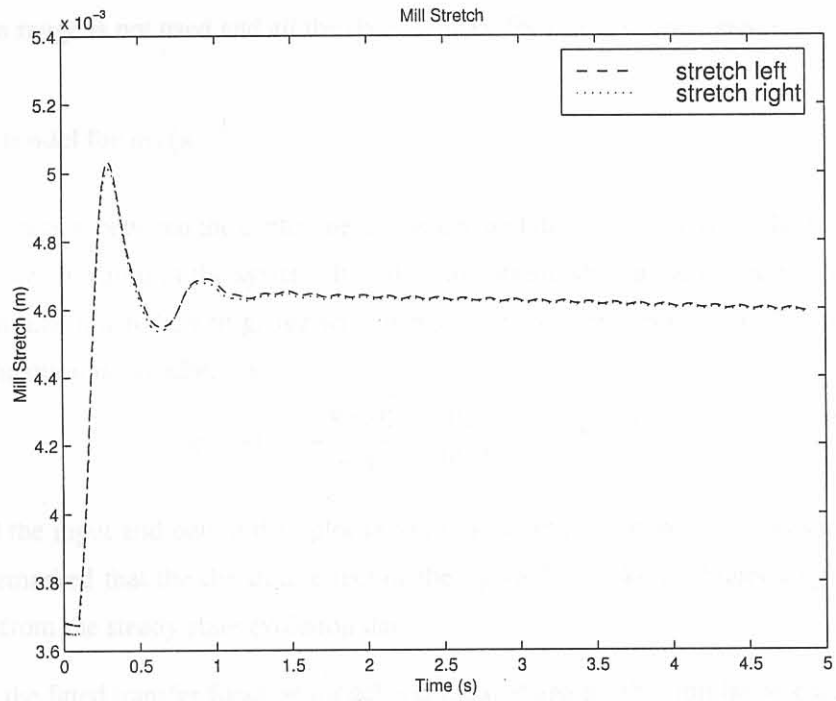

Figure 5.19: Mill stretch, after the application of a step input of $1mm$ in the hydraulic stroke at 92.6ms.

Different values for $\Delta v_{\kappa c}$ and Δt_{step} were experimented with. The two parameters were chosen as, $\Delta v_{\kappa c} = \pm 0.2 m.s^{-1}$ and $\Delta t_{step} = 60 \times 10^{-3} s$.

5.4.1.3 Input thickness disturbance, δh_1

The operating point was chosen on the speed up ramp of pass 3 and the input thickness disturbance is the controlled exit thickness of the previous pass. Thus the entrance thickness deviation will not be so large, and from the logged data of the Steckel Mill under consideration, the absolute value of the thickness deviation is less than $|200|\mu m$. In [64] the investigated hydraulic gauge control system was tested with a maximum input thickness deviation of $|200|\mu m$, which gives justification for the choice of a disturbance step input of $0.2mm$ in this dissertation.

5.4.2 Identification

The data of the applied step tests are analyzed with the aid of the System Identification toolbox of Matlab. ARX (Auto Regression with eXternal input) models were fitted [83]. In this dissertation an exposition of system identification is not given and the interested reader is referred to References [84, 83].

In section 5.3.1 a remark was made about the long duration of any simulation. This places a restriction on the amount of available data suitable for system identification purposes, and in some cases a model validation data range is not used and all the data are used for fitting of the models.

5.4.2.1 The model for $g_{11}(s)$

This transfer function between the centerline exit gauge and the requested hydraulic stroke is the most important transfer function of the system. It will be important when a model based controller is used to predict with how much the exit gauge will change when a change is made in the hydraulic stroke. The transfer function is calculated as,

$$g_{11}(s) = \frac{-8.0865 \times 10^{-2}}{s + 1.9 \times 10^{-1}} e^{-4.15 \times 10^{-3} s}. \tag{5.5}$$

In figure 5.20 the input and output data plot used in the identification of $g_{11}(s)$ is shown. In section 5.4.1.1 it is remarked that the dynamic effect of the hydraulic stroke is obtained by subtracting the step test data from the steady state evolution data.

In figure 5.21 the fitted transfer function model is compared against the simulation data obtained from the nonlinear plant simulator.

The accuracy of the identified transfer function models was done by looking at the autocorrelation function of the error between the model output and the simulation data, and the cross correlation

between this error and the manipulated variable that was stepped. The 99% confidence intervals for these correlation values are computed using the 'resid' command in Matlab's SID toolbox and are displayed as dotted lines on the correlation plots. The computation of these values is done assuming that the error to be white and independent of the stepped manipulated variable [83]. An autocorrelation and cross correlation plot obtained from identifying $g_{11}(s)$ is shown in figure 5.22. From this plot it can be seen that the cross correlation lies in the 99% confidence intervals, but the autocorrelation transgress this 99% confidence level. From this plot and the good correspondence of the time plot (figure 5.21), the transfer function model can be regarded as a good fit to the simulation data.

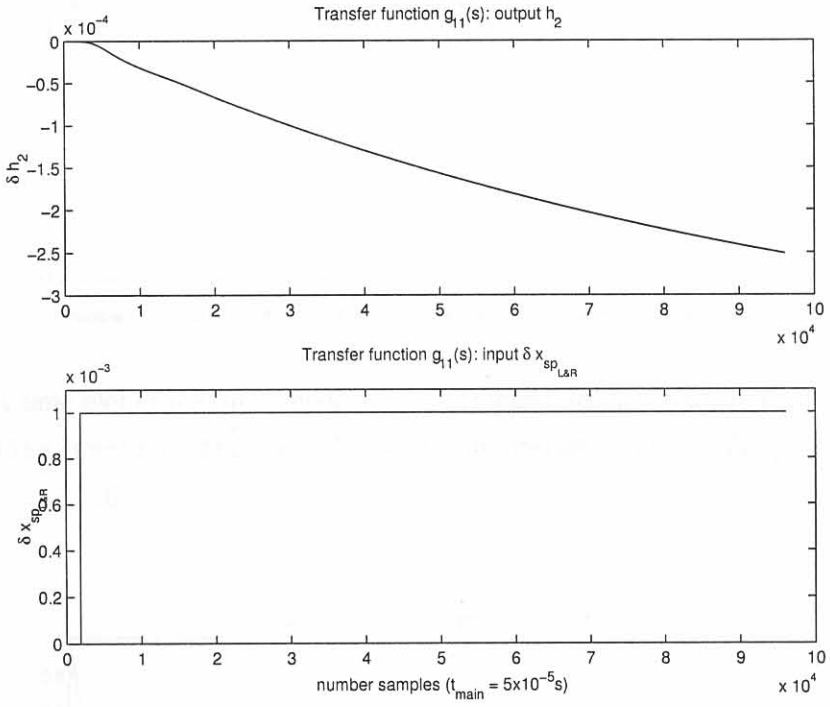

Figure 5.20: I/O data used in the identification of $g_{11}(s)$. (The x axis denotes the number of samples with the sampling interval given as $t_{main} = 5 \times 10^{-5}$)

5.4.2.2 The model for $g_{21}(s)$ and $g_{31}(s)$

The two transfer functions between the tension outputs and the hydraulic stroke setpoint are very similar. It should be noted that the fitting ranges of these two models were taken such that the tensions stayed greater than zero in the simulations. In figure 5.23 the I/O data plot used in the identification of $g_{21}(s)$ is shown. In figure 5.24 the identified transfer function model for $g_{31}(s)$ is compared to the nonlinear plant simulation data. In figure 5.25 the auto- and cross correlation plots of the identified transfer function model for $g_{21}(s)$ are shown. From these figures it can be concluded that the identified models approximate the nonlinear behaviour accurately at the point of linearization. The models are

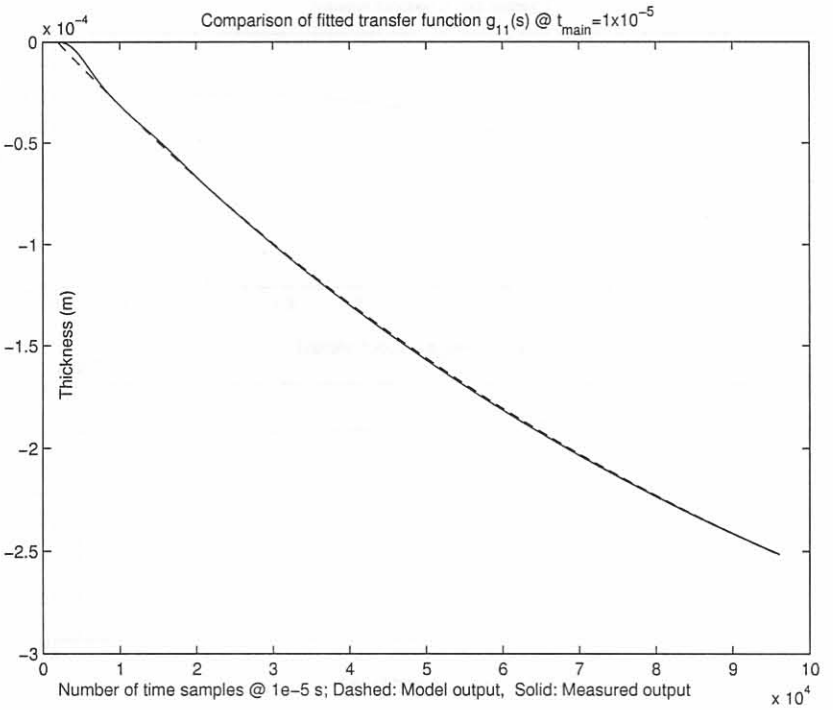

Figure 5.21: A time plot of the fitted model $g_{11}(s)$ compared to the simulation data obtained from the nonlinear plant simulator. (The x axis denotes the number of samples with the sampling interval given as $t_{main} = 5 \times 10^{-5}$)

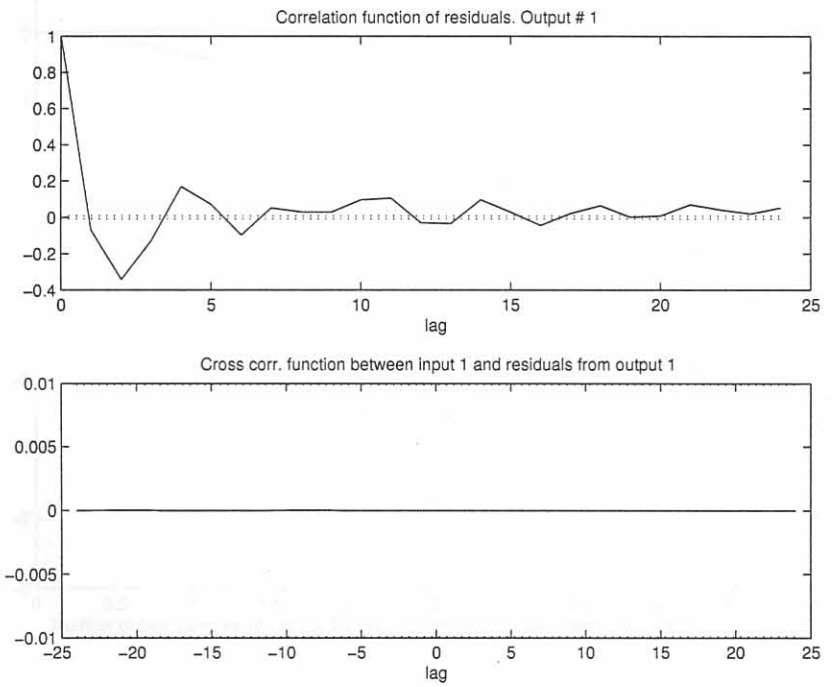

Figure 5.22: Correlation and cross correlation plots of the fitted model for $g_{11}(s)$. The dotted lines indicate the 99% confidence level.

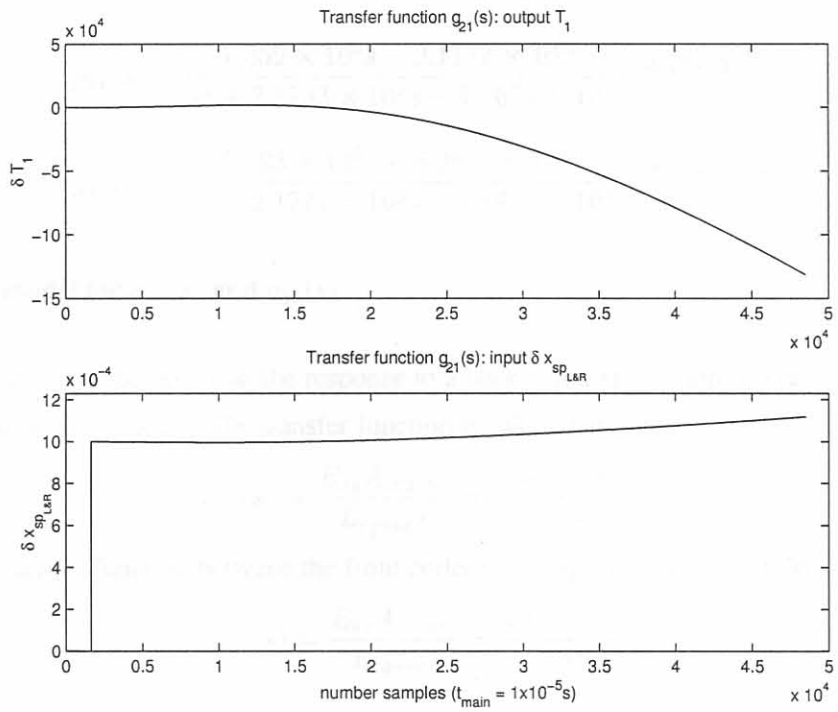

Figure 5.23: I/O data used in the identification of $g_{21}(s)$[10]. (The x axis denotes the number of samples with the sampling interval given as $t_{main} = 5 \times 10^{-5}$)

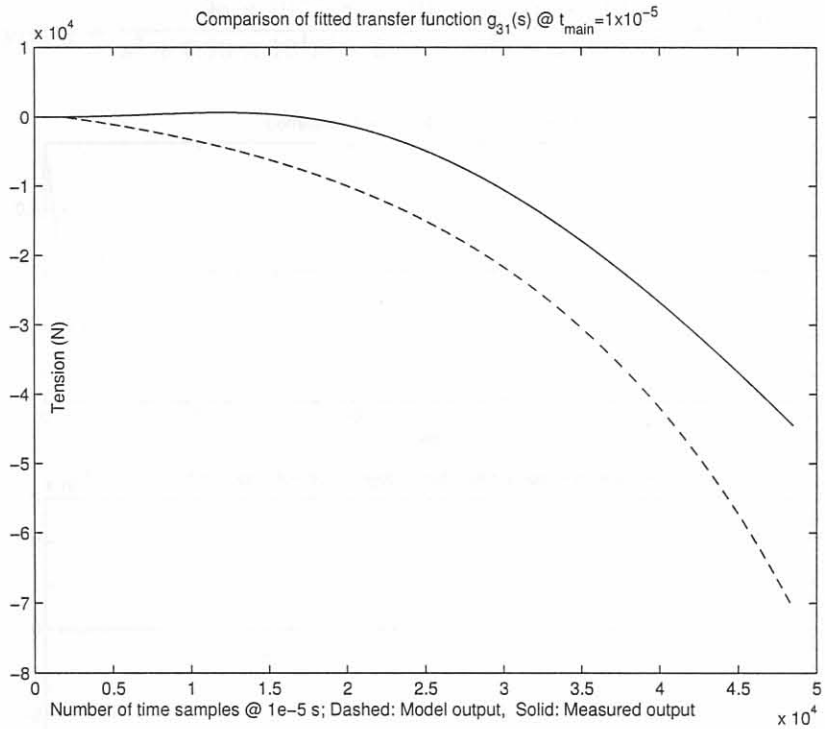

Figure 5.24: A time plot of the fitted model $g_{31}(s)$ compared to the simulation data obtained from the nonlinear plant simulator. (The x axis denotes the number of samples with the sampling interval given as $t_{main} = 5 \times 10^{-5}$)

given as,

$$g_{21}(s) = \frac{1.059 \times 10^5 s - 2.1177 \times 10^{10}}{s^2 + 2.1183 \times 10^2 s - 1.1674 \times 10^3} e^{-0.15 \times 10^{-3} s}. \tag{5.6}$$

$$g_{31}(s) = \frac{3.493 \times 10^5 s - 6.9612 \times 10^{10}}{s^2 + 2.1771 \times 10^3 s - 1.1989 \times 10^4} e^{-0.33 \times 10^{-3} s}. \tag{5.7}$$

5.4.2.3 The model for $g_{22}(s)$ and $g_{33}(s)$

From figure 5.26 it can be seen that the response to a back coiler speed step is a ramp in the tension, signalling a capacitive process. The transfer function is calculated as,

$$g_{22}(s) = \frac{E_{ss} A_{cross_1}}{L_{rg \leftrightarrow cf}} = -\frac{308 \times 10^6}{s}. \tag{5.8}$$

Similarly the transfer function between the front coiler motor speed and the strip front tension is,

$$g_{33}(s) = \frac{E_{ss} A_{cross_2}}{L_{rg \leftrightarrow cf}} = \frac{225 \times 10^6}{s}. \tag{5.9}$$

5.4.2.4 The model for $g_{12}(s)$

The transfer function was calculated as,

$$g_{12}(s) = \frac{7.96 \times 10^{-5} s^2 + 2.017 s - 5.94 \times 10^4}{s^3 + 6.93 \times 10^4 s^2 + 8.54 \times 10^8 s - 3.82 \times 10^{10}} e^{-5 \times 10^{-3} s}. \tag{5.10}$$

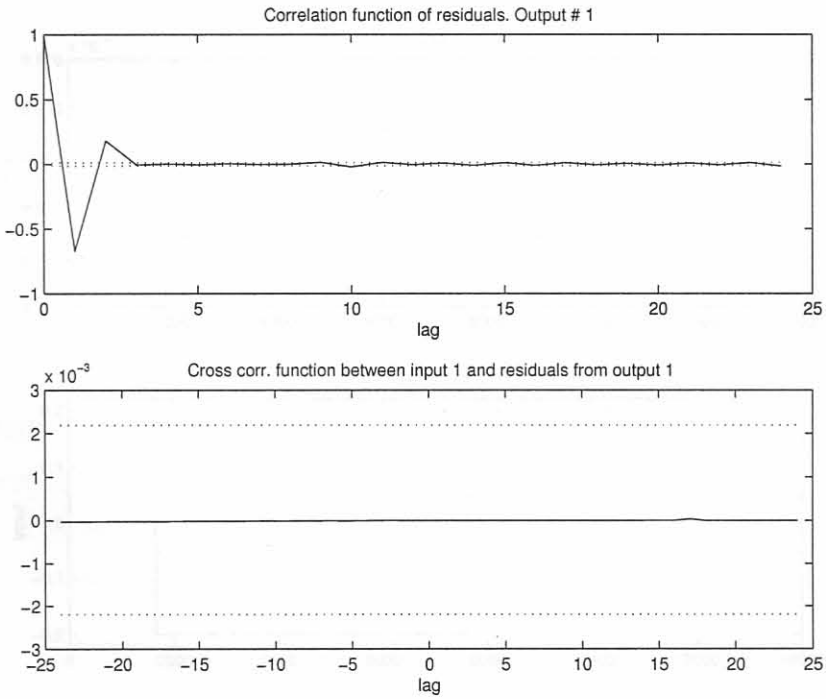

Figure 5.25: Correlation and cross correlation plots of the fitted model for $g_{21}(s)$. The dotted lines indicate the 99% confidence level.

From the time signals (figures 5.27) it can be seen that the speed inputs does influence the thickness output, but not by much. The speed inputs only start to play a role as soon as the tension start to increase above a threshold value when the tension nears the yield stress of the material. In figure 5.31 it can be seen how the application of a step on the back tension influence the centerline thickness.

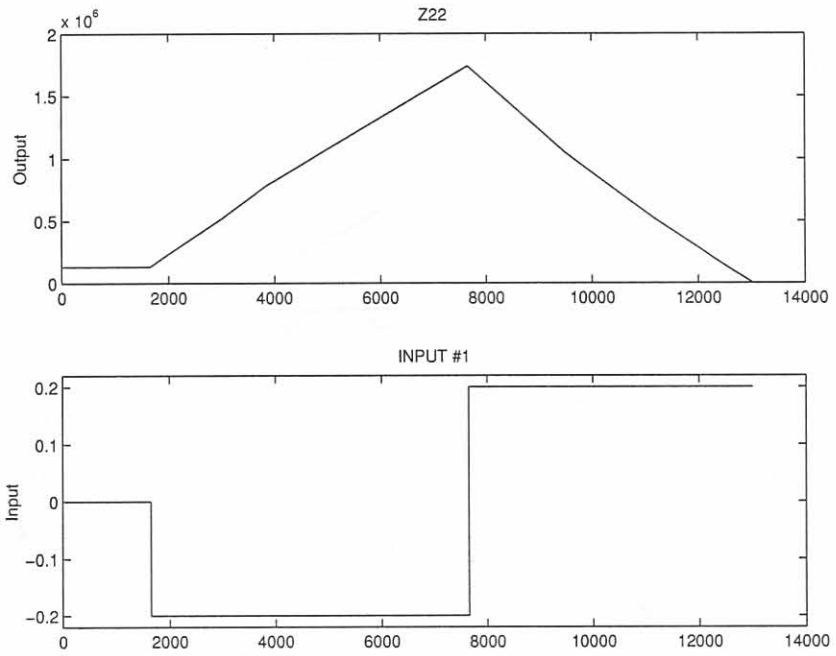

Figure 5.26: The input/output relationship for the derivation of $g_{22}(s)$. (The x axis denotes the number of samples)

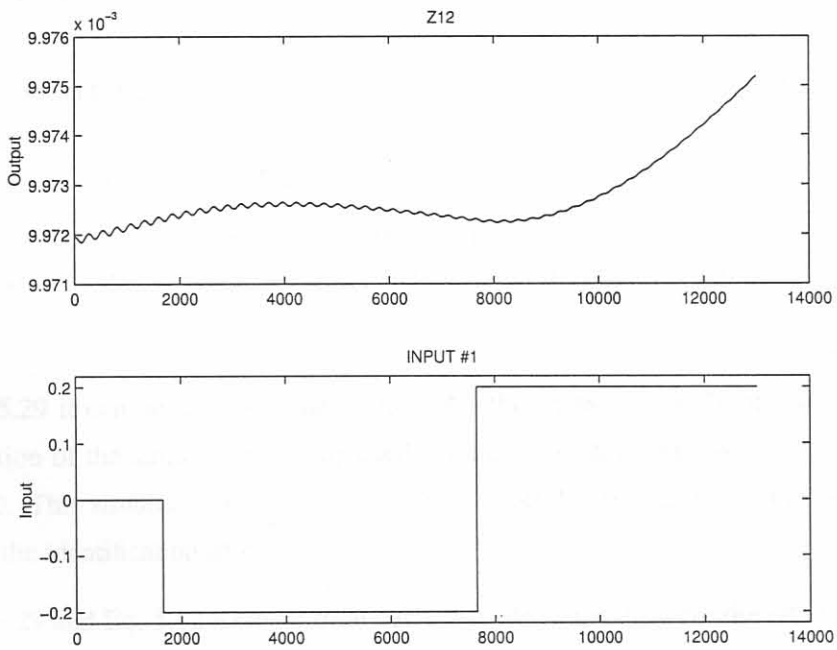

Figure 5.27: The input/output relationship for the derivation of $g_{12}(s)$. (The x axis denotes the number of samples)

5.4.2.5 The model for $g_{32}(s)$

The transfer function was calculated as,

$$g_{32}(s) = \frac{4.294 \times 10^5 s^2 - 6.82 \times 10^{10} s - 1.18 \times 10^{14}}{s^3 + 1.57 \times 10^5 s^2 - 3.19 \times 10^6 s + 2.06 \times 10^8} e^{-3.21 \times 10^{-3} s} \tag{5.11}$$

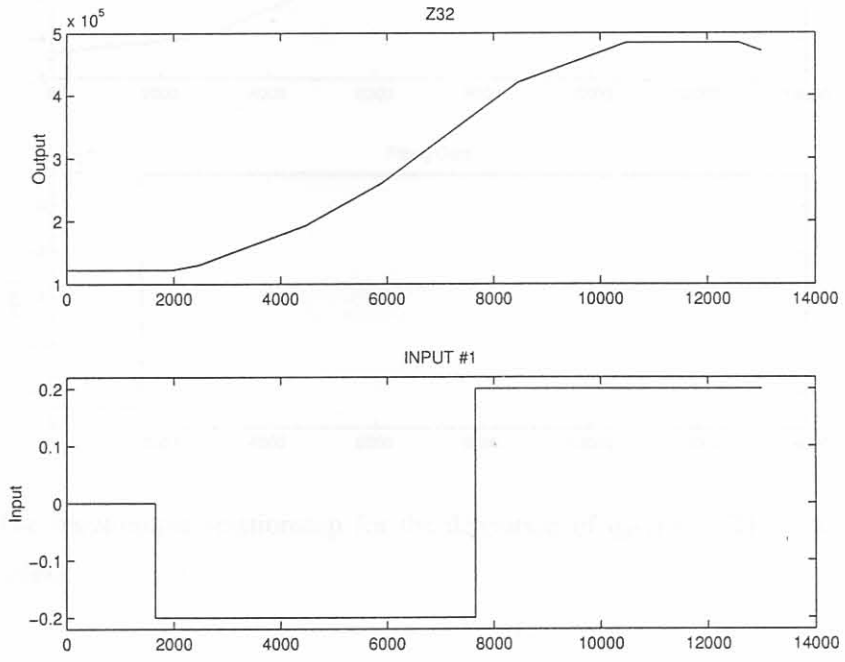

Figure 5.28: The input/output relationship for the derivation of $g_{32}(s)$. (The x axis denotes the number of samples)

5.4.2.6 The model for $g_{d11}(s)$

The transfer function was calculated as,

$$g_{d11}(s) = \frac{-1.06 \times 10^{-3} s^3 - 3.95 \times 10^2 s^2 - 4.18 \times 10^7 s - 3.74 \times 10^{13}}{s^4 + 1.0353 \times 10^5 s^3 + 1.017 \times 10^{11} s^2 + 6.24 \times 10^{14} s - 3.9 \times 10^{14}} . e^{-8.49 \times 10^{-3} s}. \tag{5.12}$$

From figure 5.29 it can be seen that the initial input thickness step of 1mm was too large for the allowed duration of the simulation. An updated simulation with an input step of $|200 \mu m|$ is shown in figure 5.30. This simulation run, was however of small duration and the obtained results do not contribute to the identification of $g_{d11}(s)$.

From figure 5.29 and Eq. 5.12 a longer time delay was identified, than for the other transfer function models. This large time delay is associated with the time necessary for the strip to travel through the roll gap (transport time). This time delay is only a fraction of the transport time, and only models the first time instance when the effect of an increased draft is detected. This associated transport time is

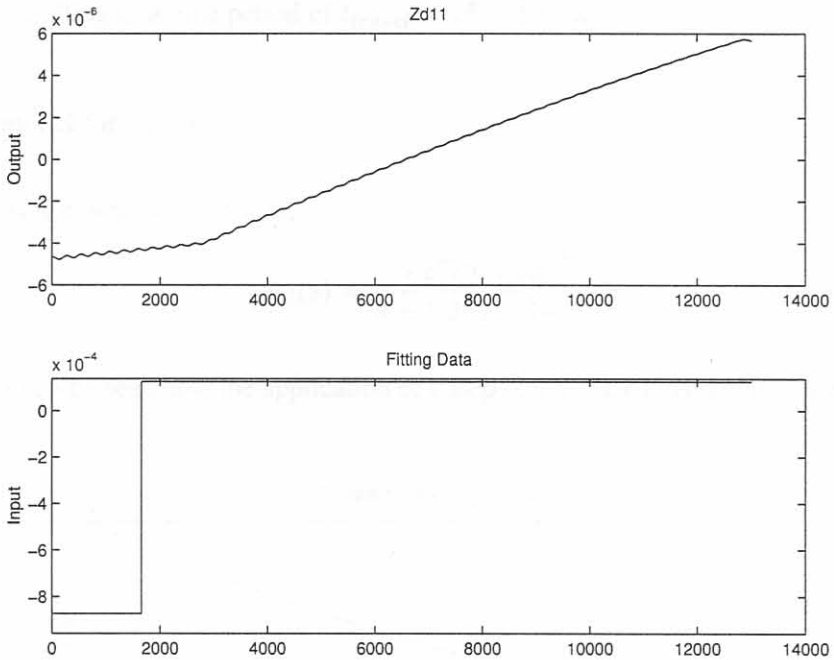

Figure 5.29: The input/output relationship for the derivation of $g_{d11}(s)$. (The x axis denotes the number of samples)

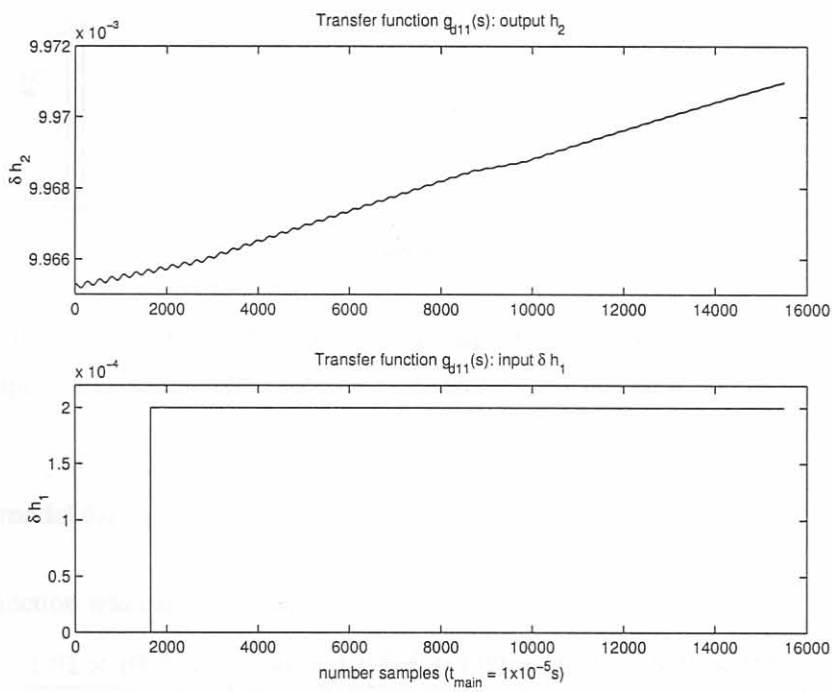

Figure 5.30: The input/output relationship for the derivation of $g_{d11}(s)$. (The x axis denotes the number of samples with the sampling interval given as $t_{main} = 5 \times 10^{-5}$)

calculated by taking the length of the arc of contact, $L_p = 0.05m$, and the operating velocity of the mill is 3.5m/s, resulting in a time period of $t_{travel} = 15 \times 10^{-3}s$.

5.4.2.7 The model for $g_{d12}(s)$

The transfer function was calculated as,

$$g_{d12}(s) = \frac{-5.2779 \times 10^{-11}}{s + 1.964 \times 10^{-1}}. \tag{5.13}$$

In figure 5.31 it can be seen how the application of a step on the back tension influence the centerline thickness.

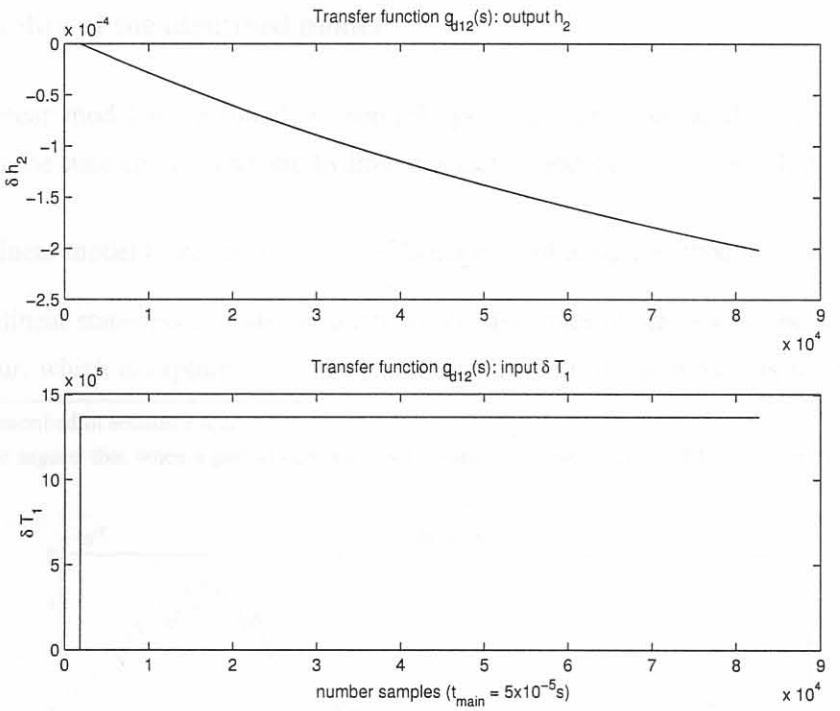

Figure 5.31: The input/output relationship for the derivation of $g_{d12}(s)$. (The x axis denotes the number of samples with the sampling interval given as $t_{main} = 5 \times 10^{-5}$))

5.4.2.8 The model for $g_{d13}(s)$

The transfer function was calculated as,

$$g_{d13}(s) = \frac{1.01 \times 10^{-11}s^3 - 2.46 \times 10^{-6}s^2 + 4.02 \times 10^{-1}s - 9.23 \times 10^3}{s^4 + 8.74 \times 10^4 s^3 + 5.61 \times 10^{10}s^2 + 1.99 \times 10^{14}s + 1.72 \times 10^{16}} e^{-1.28 \times 10^{-3}s}. \tag{5.14}$$

In figure 5.26 it can be seen how the application of a step on the back tension influence the centerline thickness.

From figures 5.31 and 5.32 which were obtained from two different types of simulations, it is evident that if the tension step is small and not of a long duration the influence on the exit gauge is small. On the other hand if a large tension step is applied and held at that value, it can be seen that the influence on the exit gauge can become more of a cumbersome factor. The results obtained from the simulation for the identification of $g_{d12}(s)$ gives justification for investigating the tension and thickness interactions. The simulation results from the identification of $g_{d13}(s)$ was applied for too short time duration and it might be necessary to repeat this experiment to obtain a better result. It also needs to be stressed that the tensions were limited, in order to prevent necking from occuring[11], when necking are modelled and allowed the attainable tension to gauge impact can be larger making tension control a necessity.

5.4.3 Suitability of the identified model

Why is this linear model more suited for control system design, compared to the nonlinear or a linearization of the state-space stand and hydraulic actuator model (e.g. not the whole simulator)?

- With a linear model there are a number of linear control design methods that can be used.
- The nonlinear state-space model accounts for the dynamics of the process, but the the material behaviour, which is captured with the simulation of the roll gap model, is not incorporated[12]

[11] Necking is described in section 3.4.2.

[12] It can also be argued that when a partial derivative with respect to time is taken of Eq. 3.15 a dynamic model can

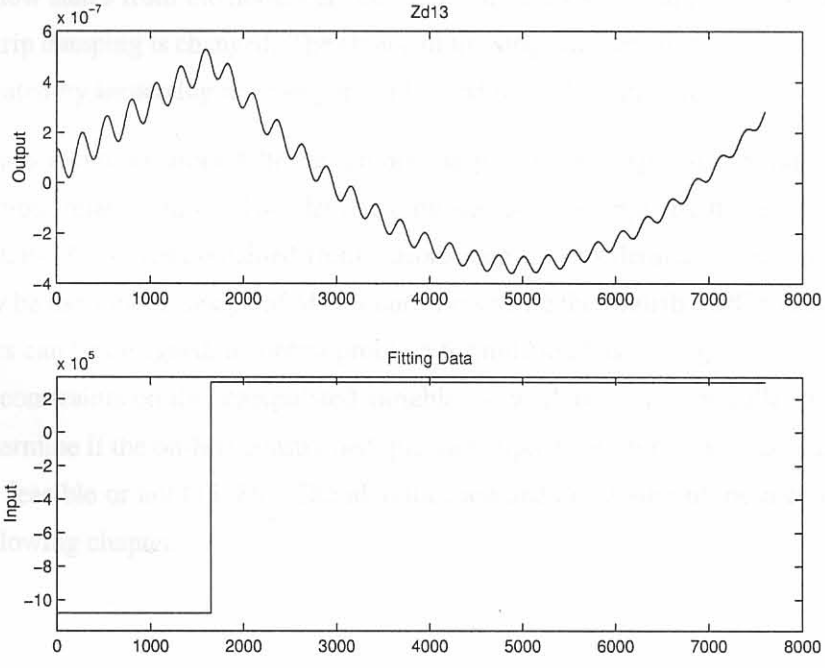

Figure 5.32: The input/output relationship for the derivation of $g_{d13}(s)$. (The x axis denotes the number of samples)

into the non-linear or a linearized version of the state-space model of the stand and the hydraulic actuators.

- The identified MIMO I/O representation does identify the dynamic behaviour of the total simulator, e.g. the dynamic behaviour of the stand and hydraulic actuators and the static interaction of the material with the rollers. This transfer function model can also easily be used with the Matlab MPC toolbox.

- The dimension of the state-space model is large (i.e. 18 states), and when the 4 roller case is of interest or when the higher frequency vibration modes also need to be modelled, the number of states of the simulator increases. This increase can possibly increase the difficulty of designing a state feedback controller in the state space domain.

5.5 Conclusion

In this chapter some simulation results were shown and the system identification process was done in order to yield a linear MIMO plant model that can be used for controller design.

As part of the simulation results, it was shown how the roll gap model unit reacts, in terms of the neutral point movement, when applied tensions to the strip are modelled. Results showed how the specific rolling force change when the draft input and applied tensions were varied. These relationships were compared to the physical limits of the mill.

It was shown how states from the nonlinear state-space model vary at supposedly steady state, when values of the strip damping is changed. The choice of the strip damping that was used in the simulator was also motivated by inspecting the damping ratios and natural frequencies of the stand model.

A linear plant was identified around the chosen operating point and expressed in transfer function notation (input/output relationships). The identification was done by applying the System Identification toolbox of Matlab [83] to data obtained from various step tests as defined in this chapter. The total model can now be used in the design of MPC controllers using the Matlab MPC toolbox [85]. Before such controllers can be designed, a control problem formulation has to be given. An industrial MPC controller has constraints on the manipulated variables as well as on the controlled variables. These constraints determine if the on-line constrained quadratic optimization problem associated with MPC controllers are feasible or not [15, 86]. The identification and discussion of these constraints will be done in the following chapter.

be constructed for the material behaviour. This dynamic model can be incorporated into the nonlinear state-space model, making it more suitable for state-space controller design.